Advanced Steel Construction – Vol. 20 No. 4 (2024) 385–396
DOI: 10.18057/IJASC.2024.20.4.6

RESEARCH ON DATA-DRIVEN INTELLIGENT DESIGN METHOD FOR ENERGY DISSIPATOR OF FLEXIBLE PROTECTION SYSTEMS

Ze-Huan He [1], Zhi-Xiang Yu [1, 2, *], Lin-Xu Liao [1] , Yang-Feng Lyu [1] and Yong-Ding Tian [1]

[1] *School of Civil Engineering, Southwest Jiaotong University, Chengdu, China*
[2] *National Engineering Laboratory for Prevention and Control of Geological Disasters in Land Transportation, Chengdu, China*
** (Corresponding author: E-mail: yzxswjtu@163.com)*

ABSTRACT

The brake ring, an essential buffer and energy dissipator within flexible protection systems for mitigating dynamic impacts from rockfall collapses, presents notable design challenges due to its significant deformation and strain characteristics. This study introduces a highly efficient and precise neural network model tailored for the design of brake rings, utilizing BP neural networks in conjunction with Particle Swarm Optimization (PSO) algorithms. The paper studies the key geometric parameters, including ring diameter, tube diameter, wall thickness, and aluminum sleeve length, with performance objectives centered on starting load, maximum load, and energy dissipation. A comprehensive dataset comprising 576 samples was generated through the integration of full-scale tests and simulations, which facilitated the training of the neural network for accurate forward predictions linking physical parameters to performance outcomes. Furthermore, a PSO-based reverse design model was developed to enable effective back-calculation from desired performance outcomes to specific geometric configurations. The BP neural network exhibited high accuracy, evidenced by a fit of 0.991, and the mechanical performance of the designed products aligned with target values in over 90% of cases, with all engineering errors remaining within acceptable limits. The proposed method significantly reduces the design time to under 5 seconds, thereby vastly improving efficiency in comparison to traditional approaches. This advancement offers a rapid and reliable reference for the design of critical components in flexible protection systems.

ARTICLE HISTORY

Received: 10 March 2024
Revised: 9 August 2024
Accepted: 5 September 2024

KEYWORDS

Flexible protective systems;
Energy dissipator;
Brake ring;
Data-driven;
Intelligent design

Copyright © 2024 by The Hong Kong Institute of Steel Construction. All rights reserved.

1. Introduction

Flexible protection systems are widely used in rockfall protection projects along transportation routes [1-3], with the energy dissipator serving as a critical component. When subjected to dynamic impacts, the energy dissipator is activated by the high tension in the ropes, functioning similarly to the hydraulic buffering devices in aircraft carrier arresting systems. Its simplicity and efficiency make it an indispensable part of flexible protection systems. Muraishi et al.[4] demonstrated that energy dissipators could enhance the protective performance of flexible protection systems by more than threefold, with the contribution ratio of energy dissipators to the performance of flexible protection systems exceeding 60%. Therefore, energy dissipators are essential for flexible protection systems under strong impacts, making their proper design crucial for protection success. Currently, brake rings are commonly used as energy dissipators in flexible protection systems. They consist mainly of circular steel tubes and aluminum sleeves (see Fig. 1). When the wire ropes pass through these tubes and are pulled tight, they cause them to bend and deform, creating an energy-absorbing mechanism that enhances the system's protective performance (see Fig. 2).

Numerous scholars have extensively researched various forms to advance the scientific design of energy dissipators. Fresno et al.[5] performed mechanical experiments on double U-shaped energy dissipators, exploring their energy absorption capabilities and conducting finite element analysis. Their findings suggest that these energy dissipators exhibit enhanced energy absorption under asymmetric tensile loads at a 2/3 ratio. Lamber et al.[6] investigated a novel tubular buckling energy dissipator through model tests and numerical simulations. They discovered this new dissipator type is more effective and exhibits greater energy absorption than friction-type dissipators. J.J.Del Coz Díaz et al.[7] used numerical simulations and model experiments to study the mechanical behavior of U-shaped ring energy dissipators. They identified that the failure mode was due to the compression damage of the aluminum sleeves. Castanon-Jano et al.[8] systematically analyzed the roles and mechanical behaviors of various energy dissipators in flexible protection systems. Qi Xin et al.[9] conducted drop-weight impact dynamic tests on brake rings and proposed a four-stage mechanical model under dynamic loads. The aforementioned studies have revealed the quasi-static and dynamic mechanisms of various energy dissipators. They have identified key parameters affecting mechanical performance and addressed challenges in simulating large deformations, geometric nonlinearity, and material nonlinearity. These insights provide a solid foundation for designing energy dissipators. However, existing design methods are limited by high experimental costs and complex theoretical calculations, hindering the practical application of energy dissipators. A fast and precise design method has long been lacking in engineering.

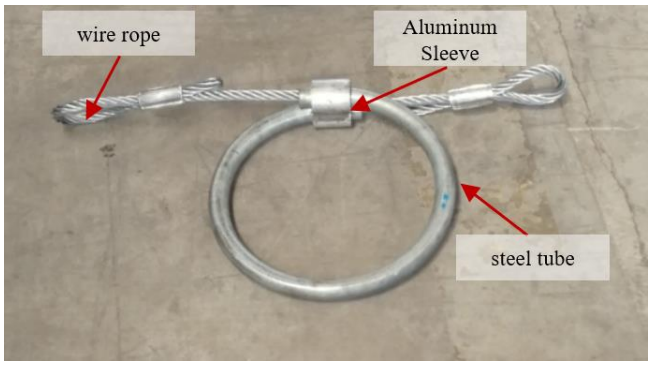

Fig. 1 The brake ring

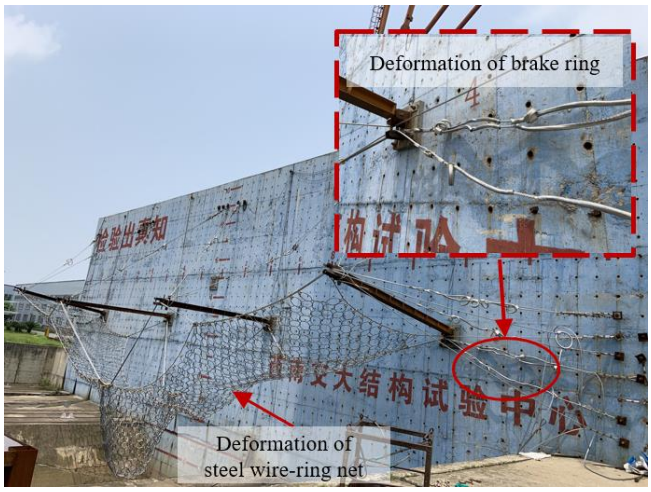

Fig. 2 Deformation of flexible protection systems by impact

The application of artificial intelligence (AI) technology in structural engineering design has witnessed a significant surge in recent years, thus emerging as a prominent area of research focus[10-15]. The AI algorithms, with their self-learning and parallel processing capabilities, effectively establish mathematical models linking complex input parameters to design outcomes.

This approach circumvents the decoupled calculations of complex engineering mechanics [16-18], freeing engineers from intricate computations and enabling efficient, accurate designs. Among various AI algorithms, the backpropagation (BP) neural network stands out for its ability to automatically optimize models through the backpropagation algorithm, requiring only the forward process to be differentiable. Ma Gao et al.[19] used a BP neural network to predict the compressive strength of CFRP-confined concrete. The number of data points with an error within 15% was increased by 20% compared to traditional statistical regression. Zhou Zhong et al.[20] successfully used a BP neural network optimized with Particle Swarm Optimization (PSO) to predict the turbidity levels of wastewater from tunnel construction processes.

In the field of flexible protection engineering, LIAO et al.[21] have pioneered the application of neural networks, developing an intelligent computational method that achieves complex nonlinear mapping between system performance and structural components. Given the strong non-linear characteristics of flexible protection engineering, neural networks offer a more efficient and comprehensible means to map the intricate relationships between protection performance and various structural parameters [22,23]. Despite these advancements, intelligent design methods for both individual components and entire flexible protection systems remain largely unexplored. Therefore, researching intelligent design methods for flexible protection engineering is crucial for developing precise and efficient protection solutions.

Consequently, this paper centers on energy dissipators in flexible protection systems, providing a theoretical analysis of their contribution to the system and the influence of their structural parameters on protection performance. In practical application, this study integrates finite element analysis with intelligent algorithms, employing LS-DYNA software for simulations and analyzing data using BP neural networks and particle swarm optimization (PSO) algorithms. A novel data-driven energy dissipator design method was developed, validated through physical testing to enhance design precision and efficiency. Compared to traditional methods, the proposed approach offers high efficiency and automation. The comprehensive process comparison illustrated in Fig. 3.

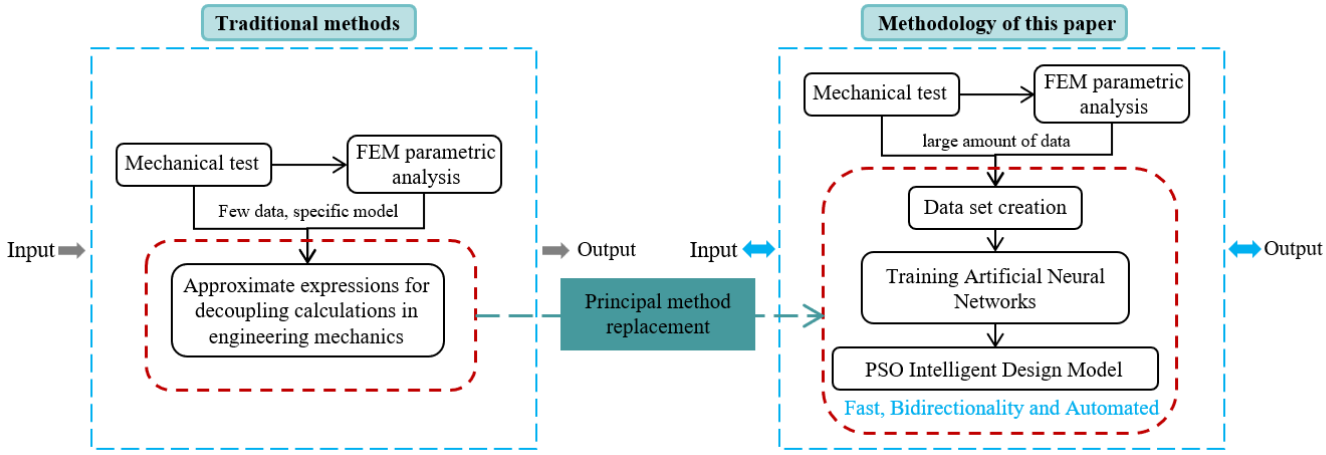

Fig. 3 Comparison of technical approaches

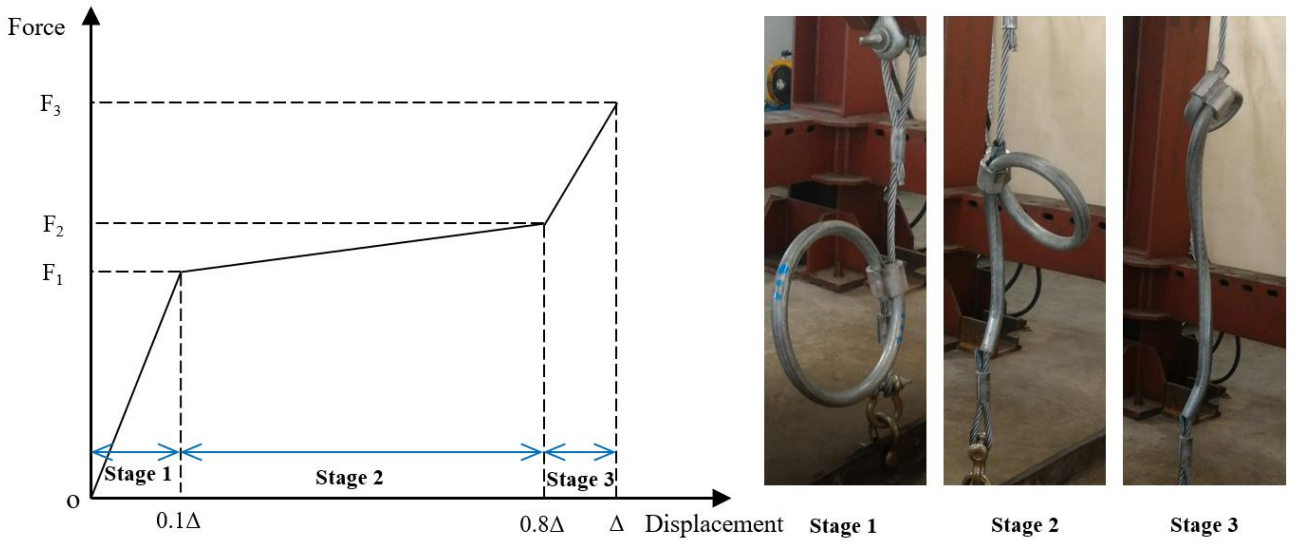

Fig. 4 The Trilinear model of the load-displacement curve and its corresponding stage deformation of brake ring

2. Data set creation

2.1. Principle of brake ring operation

When the system impacts, the rope experiences high tension, which activates the brake ring. Despite variations in construction, different types of energy dissipators generally absorb energy through friction and plastic deformation. For instance, the brake ring's working phase primarily involves the bending-straightening deformation of the steel tube and the sliding friction deformation through the aluminum sleeve, collectively forming a pseudo-plastic P-D mechanism. When the steel tube stretches to its maximum length, the brake ring will strengthen and eventually break. In practical engineering, the effective sliding distance Δ is typically considered to be 0.7 times the circumference of the brake ring. The energy absorption process of the brake ring can be divided into three distinct stages. Phase One: The tensile force of the steel wire rope rapidly increases, overcoming the friction between the aluminum sleeve and the steel tube. During this phase, minimal displacement occurs as static friction is overcome, with corresponding displacement at 0-0.1Δ. Phase Two: The tensile force of the steel wire rope overcomes static friction, causing relative displacement between the steel tube and the aluminum sleeve. Overcoming static friction results in a sudden drop in the load. As the relative displacement progresses, the diameter of the brake ring gradually decreases,

while the stiffness and constraining ability of the aluminum sleeve increase, causing a slow increase in load, with corresponding displacement at 0.1-0.8Δ. Phase Three: When the brake ring contracts to a certain extent, the steel tube undergoes torsional deformation, increasing the contact force between the aluminum sleeve and the steel tube. This leads to a significant increase in load during the final phase, with displacement increasing slowly until failure occurs, corresponding to a displacement of 0.8-1Δ (see Fig. 4).

The main factors influencing friction energy dissipation include the compression force P_t during deformation, the dynamic friction coefficient μ, the length of the aluminum sleeve L, the diameter of the steel tube ring D, and the diameter of the steel tube d. The specific geometric parameters are depicted in Fig. 5.

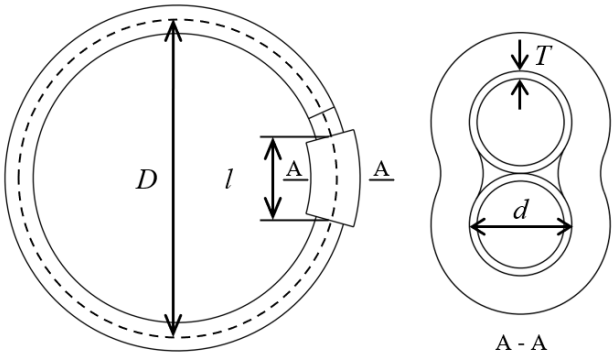

Fig. 5 Structural parameters of the brake ring

As the dynamic friction coefficient μ remains constant, the compressive force during deformation is primarily determined by the dimensions of the steel tube and the aluminum sleeve. Therefore, the friction energy dissipation W_1 can be represented as a function related to time t:

$$W_1 = f(P_t, L, D, d, T, t) \tag{1}$$

In the deformation energy dissipation phase, the steel tube experiences bending and straightening deformation. The primary factors influencing this process are the wall thickness T and the diameter d of the steel tube. Consequently, the deformation energy dissipation W_2 can be described as a function of time t:

$$W_2 = g(T, d, t) \tag{2}$$

In conclusion, the total energy dissipation W of the brake ring can be expressed as:

$$W = W_1 + W_2 = f(P_t, L, D, d, T, t) + g(T, d, t) \tag{3}$$

From the above equation, the primary factors influencing the protective performance of the brake ring, considering its structural dimensions, are the ring diameter D, tube diameter d, steel tube wall thickness T, and length of the aluminum sleeve L.

2.2. Calibration of numerical models

The elongation process of the brake ring exhibits large deformation effects and involves complex forces, addressing issues of geometric and material nonlinearity. This paper employs the numerical simulation method for brake rings using LS-DYNA, as applied in several studies[24-26].

In the numerical simulation, the aluminum sleeve is modeled using solid elements with the default single-point integration algorithm. The steel tube is modeled using shell elements with the default Belytschko-Tsay single-point integration algorithm. The wire rope, subjected only to axial loads during tension and not to bending moment loads, is modeled using beam elements with the truss integration algorithm.

During the deformation of the brake ring, there is a complex contact relationship between the steel tube, aluminum sleeve, and wire rope. In LS-DYNA software, automatic surface-to-surface contact is used to account for all possible contact surfaces between different parts. This approach significantly aids in calculating the large deformations of the brake ring and enhances computational accuracy. The static and dynamic friction coefficients between steel tubes and wire ropes are 0.15 and 0.1, respectively, while those between steel tubes and aluminum sleeves are 0.18 and 0.15, respectively.

In selecting material models, an elastic material model is used for the wire rope, which often remains in the elastic stage. In contrast, elastoplastic material models are applied for the aluminum sleeve and steel tube, which undergo significant plastic strain during deformation. During the calculation process, the effects of the material hardening stage are not considered. The tangent modulus for both the steel tube and aluminum sleeve is assumed to be zero.

When the brake ring stretches at a lower speed, numerical calculations closely match the mechanical test results[11]. Considering the relevant brake ring experiments and computation time, a loading speed of 5 m/s is adopted to simulate the mechanical testing process.

Table 1 shows the material model parameters used in the calibration model for the numerical simulation. The geometric dimensions of the brake ring used in the numerical simulation calibration are: ring diameter 450 mm, tube diameter 25 mm, tube wall thickness 2.5 mm, aluminum sleeve length 60 mm, and sleeve thickness 15 mm.

Fig. 6 compares the load-displacement curves between the numerical simulation and test results. The errors for the three mechanical properties of the brake ring between the numerical simulation and test results were 9.0%, 3.7%, and 2.6%, respectively, all within the acceptable range for engineering applications. Table 2 presents the error analysis of the numerical simulation and experimental results. Following the calibration of the numerical model, parameter analysis is performed based on four influencing factors of the brake ring's structural dimensions: ring diameter D, tube diameter d, wall thickness T, and aluminum sleeve length L. Based on the calibrated model, sixteen different analysis models numbered E1 to E16 are established, with their specific parameters and performances summarized in Table 3.

Table 1
Parameters of material mechanical properties

Component	Elastic modulus (GPa)	Density (kg·m^{-3})	Yield strength (MPa)	Poisson's ratio	limit strain
Steel tube	210	7850	300	0.3	0.38
Aluminum sleeve	70	2700	235	0.3	--
wire rope	112	7850	1082	0.3	--

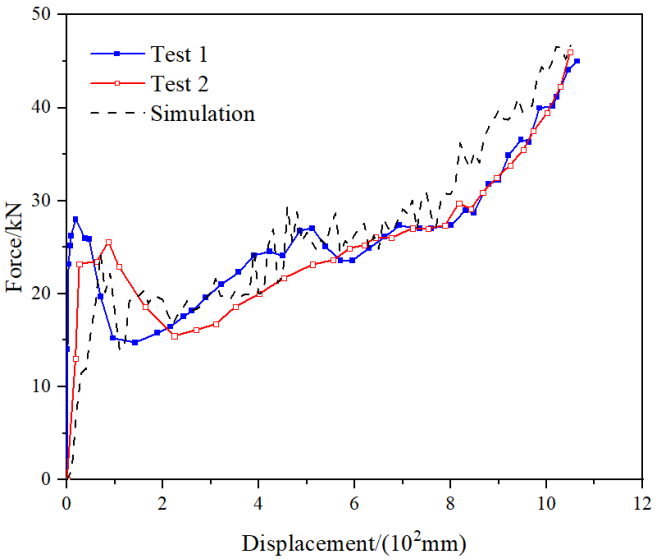

Fig. 6 Load-displacement curves from mechanical tests and numerical simulation of brake ring[24]

Table 2
Analysis of mechanical test and numerical simulation results of brake ring

Item	Starting load F_1	Maximum load F_3	Energy dissipation E
Test 1	28.0	27.3	45.0
Test 2	25.4	26.0	46.0
Test Average	26.7	26.7	45.5
Simulation	24.3	27.7	46.7
error	-9.0%	3.7%	2.6%

2.3. Effect of ring diameter on the performance of brake ring

The ring diameter *D* determines the the maximum displacement stroke of the brake ring and influences the friction and deformation energy consumption of the steel tube. Fig. 7 illustrates the load-displacement curves for four different steel tube diameter models, E1 to E4.

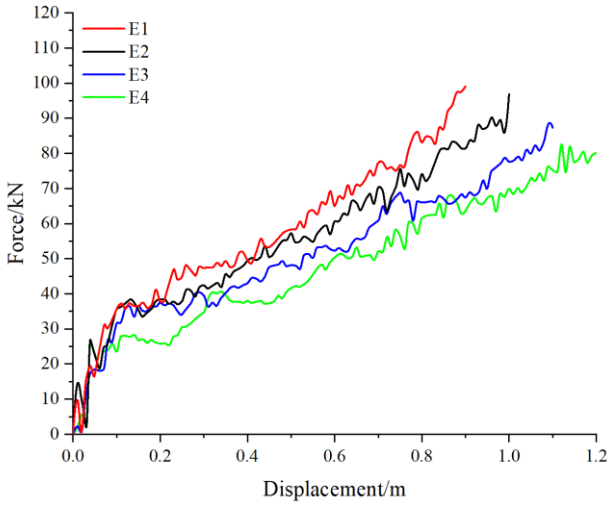

Fig. 7 Load-displacement curves of brake ring with different ring diameters

As shown in Fig. 7, within the effective displacement range, brake rings with smaller diameters *D* exhibit a more distinct three-phase trend in the load-displacement curve. For the two larger ring diameters, the third-phase trend is less distinct and resembles the slope of the second phase. Table 3 indicates that as the ring diameter increases, the starting load and maximum load decrease, while the energy dissipation slightly increases. These results suggest that increasing the diameter of the brake ring increases the effective displacement stroke but reduces the stiffness, leading to a reduction in load. Since the effective displacement is 0.7 times the circumference, larger ring diameters result in more redundant displacement, leading to less pronounced constraints in the third phase and a less evident rapid load increase.

2.4. Effect of tube diameter on the performance of brake ring

The tube diameter *d* of the steel pipe determines the contact area with the aluminum sleeve and the stiffness of the cross-section, impacting friction and deformation energy dissipation. Fig. 8 illustrates the load-displacement curves for six models with different tube diameters: E2 and E5-E9.

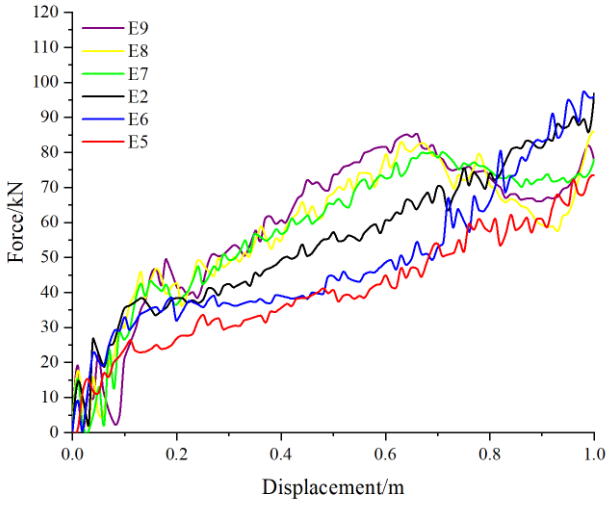

Fig. 8 Load-displacement curves of brake ring with different tube diameters

As shown in Fig. 8, within the effective displacement range, smaller tube diameters display a clear three-phase characteristic in the load-displacement curve. With increasing tube diameter, the load-displacement curve's second phase exhibits a 'bulging' phenomenon, where the load initially increases and then decreases. As shown in Table 3, with an increase in the steel tube's diameter, the contact area with the aluminum sleeve expands, the starting load rises, and energy dissipation increases from 40.8kJ to 59.4kJ, marking a 45.6% rise. For larger tube diameters, the steel tube is more severely flattened in the second phase, leading to a greater reduction in stiffness. Consequently, the load decreases, forming a convex curve. These results indicate that while increasing the tube diameter significantly enhances the brake ring's starting load and energy dissipation capacity, an excessively large diameter causes the convex curve phenomenon, lacking a distinct three-phase characteristic.

2.5. Effect of wall thickness on the performance of brake ring

The wall thickness of the steel tube influences its cross-sectional stiffness and the amount of energy dissipated through deformation. Fig. 9 illustrates the load-displacement curves of four models with different steel tube wall thicknesses, E2 and E10-E12.

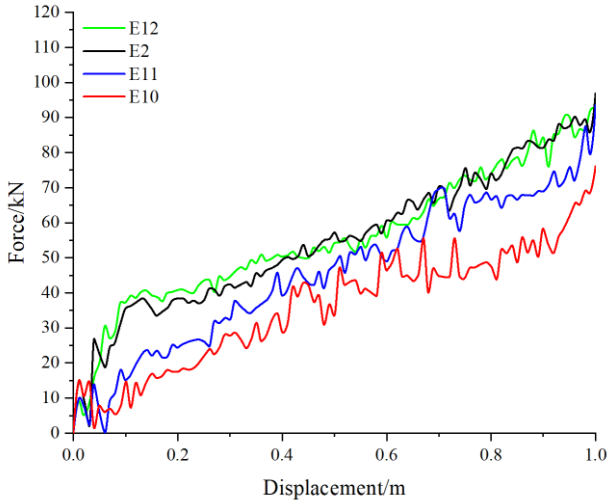

Fig. 9 Load-displacement curves of brake ring with different wall thickness

As shown in Fig. 9, the load-displacement curves of the two models with thinner walls clearly exhibit three distinct phases. For models with thicker steel tube walls, the increased sectional stiffness results in more pronounced aluminum sleeve deformation in the later stages. This reduces the aluminum sleeve's ability to restrain the steel tube during the third phase, leading to the absence of a clear third phase in the load-displacement curve. Results in Table 3 indicate that increasing the wall thickness of the steel tube significantly raises the starting load, maximum load, and energy dissipation. When the wall thickness increases from 2mm to 5mm, the starting load, maximum load, and energy dissipation rise by 140.2%, 20.9%, and 53.7%, respectively. These results demonstrate that increasing the wall thickness of the steel tube significantly enhances the brake ring's energy dissipation capacity.

2.6. Effect of aluminum sleeve length on the performance of brake ring

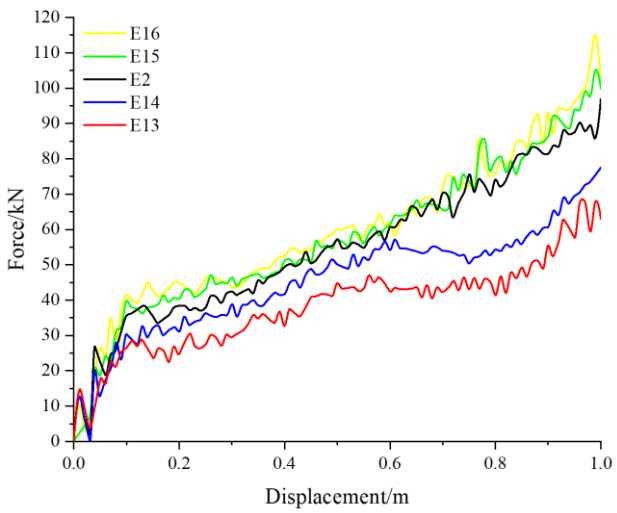

Fig. 10 Load-displacement curves of brake ring with different aluminum sleeve lengths

The length of the aluminum sleeve determines the contact area between the

steel tube and the aluminum sleeve and its ability to constrain the steel tube, thereby influencing the brake ring's friction and energy dissipation. The load-displacement curves for five models with varying aluminum sleeve lengths (E2, E13-E16) are shown in Fig. 10.

Fig. 10 shows that the load-displacement curve of the brake ring generally follows a three-phase change pattern. Longer aluminum sleeves exert stronger constraints on the steel tube, enabling earlier restraint during displacement compared to shorter sleeves. Therefore, the three models with longer aluminum sleeves exhibit weaker third-phase characteristics compared to the two models with shorter sleeves. Table 3 shows that the starting load, maximum load, and energy dissipation significantly increase with the length of the aluminum sleeve. However, for aluminum sleeve lengths within the range of 50-80mm, changes in the brake ring's starting load, maximum load, and energy dissipation are more pronounced. Beyond 80mm, the performance of the brake ring shows little change.

Table 3
Partial data set input and output parameters

Model	Variables	Brake ring dimensions				Mechanical properties		
		D(mm)	d(mm)	T(mm)	L(mm)	F_1(kN)	F_3(kN)	E(kJ)
E1	Ring diameter D	400	36	4	80	37.2	99.1	50.7
E2		450	36	4	80	38.3	96.8	55.0
E3		500	36	4	80	36.4	88.3	56.7
E4		550	36	4	80	28.0	82.5	58.3
E5	Tube diameter d	450	30	4	80	26.3	73.4	40.8
E6		450	33	4	80	33.0	97.4	49.0
E2		450	36	4	80	38.3	96.8	55.0
E7		450	44	4	80	43.3	80.1	57.8
E8		450	47	4	80	45.9	85.9	57.5
E9		450	50	4	80	46.7	85.3	59.4
E10	Wall thickness T	450	36	2	80	16.9	76.1	36.1
E11		450	36	3	80	23.7	59.7	45.7
E2		450	36	4	80	38.3	96.8	55.0
E12		450	36	5	80	40.6	92	55.5
E13	Aluminum sleeve length L	450	36	4	50	28.7	67.9	38.3
E14		450	36	4	65	32.6	77.5	45.4
E2		450	36	4	80	38.3	96.8	55.0
E15		450	36	4	90	39.8	105.1	57.5
E16		450	36	4	100	42.7	115	59.5

3. Data set creation

3.1. Combination of parameters

As analyzed in the previous section, the four structural dimension parameters of the brake ring each impact its performance differently. However, discerning the actual trends based solely on single-parameter analysis is challenging. For example, the significant impact range of the aluminum sleeve length on the brake ring's performance may vary with changes in the steel tube's diameter and wall thickness. Single-parameter analysis fails to describe the variation patterns when multiple parameters are coupled. Therefore, establishing a dataset with extensive parameter variations is more helpful for studying the patterns of how the brake ring's structural dimensions affect its performance.

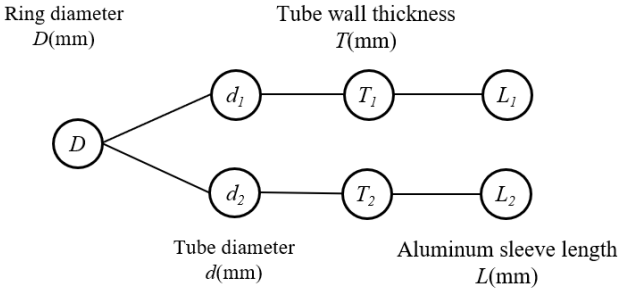

Fig. 11 Brake ring structure size combination of the numerical simulation data set

In establishing the brake ring dataset, commonly used engineering specifications were thoroughly considered. Among the structural dimensions, increasing the tube diameter decreases cross-sectional stiffness. Therefore, for larger tube diameters of 44mm, 47mm, and 50mm, greater wall thickness and longer aluminum sleeves are used to enhance sectional stiffness and constraining ability. Based on this, combinations of the four structural dimension parameters are illustrated in Fig. 11 and Table 4. After combining various structural dimensions, a total of 576 calculation conditions were obtained.

Table 4
Brake ring structure dimension parameters of numerical simulation

D(mm)	d(mm)		T(mm)		L(mm)	
	d_1	d_2	T_1	T_2	L_1	L_2
400	30		2		50	
450	33		3	3	65	65
500	36		4	4	70	80
550		44	5	5	80	90
		47		6	90	100
		50			100	110
						120

After completing the numerical calculations, extract the load-displacement curve results for all calculated conditions and fit the tri-linear load-displacement curve within the effective sliding distance[6]. Here, F_1 represents the starting load to activate the brake ring; F_3 is the maximum load within the effective sliding distance; the energy dissipation E is derived from the area under the load-displacement curve. For F_2, it must ensure that the area enclosed by the

three linear segments and the load-displacement curve equals the area above the displacement axis. Finally, the starting load F_1, maximum load F_3, and energy dissipation E are selected as the mechanical performance indicators. The curve fitting results of the numerical simulation are shown in Fig. 12.

3.2. Normalization of data sets

Considering the significant variation in the magnitudes of parameters in the dataset, it is a common practice to normalize the data before training the neural network. This study employs the Min-Max Scaling method to normalize features to the [0-1] range. This normalization simplifies the complexity of model training, enables rapid and stable training of the neural network, prevents gradient issues, and enhances the model's generalizability and interpretability.

$$x_{norm} = \frac{x - x_{\min}}{x_{\max} - x_{\min}} \tag{4}$$

where, x_{norm} is the normalized feature value; x is the actual feature value; x_{max} and x_{min} are the maximum and minimum values of the feature, respectively.

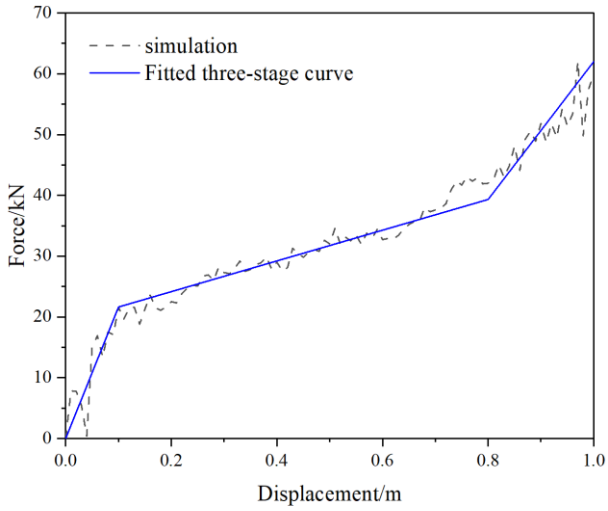

Fig. 12 Trilinear load-displacement curve within effective displacement of brake ring

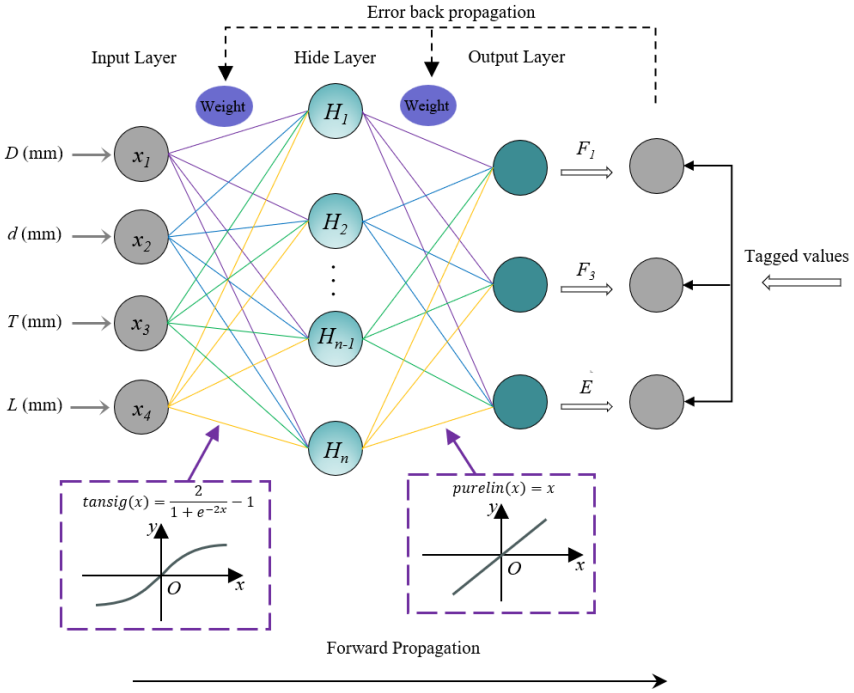

(a) BP neural network structure

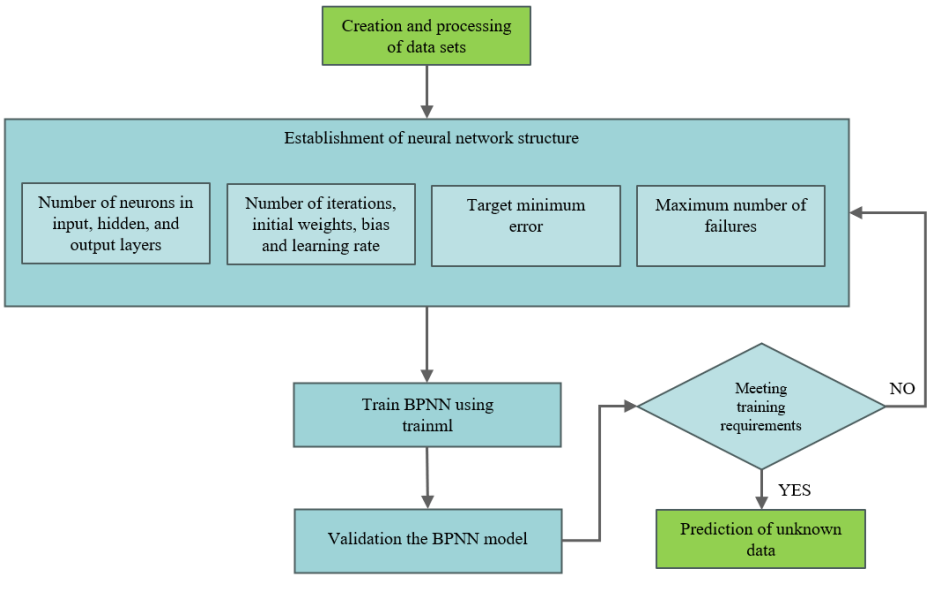

(b) BPNN Flowchart

Fig. 13 Network structure and flow chart of BPNN

4. BP neural network prediction modeling

4.1. BP neural network

The Backpropagation (BP) algorithm is a fundamental training method in deep learning, especially used in Multilayer Perceptrons (MLP). Its fundamental principle relies on supervised learning, calculating the error between the network's output and the actual target, and then adjusting the network's weights layer by layer from the output back to the input layer based on this error. This process uses the chain rule to differentiate the error, determining the direction for weight updates.

The BP neural network is composed of three types of layers: input, hidden, and output layers (see Fig. 13). Each iteration of the BP algorithm involves two main phases: forward propagation and backward propagation.

During forward propagation, sample data passes from the input layer, through the hidden layer, to the output layer (Equations 5 and 7). Activation functions (Equations 6 and 8) are then applied to generate predictions.

$$z_h = W_h \cdot x + b_h \tag{5}$$

$$a_h = \sigma(z_h) \tag{6}$$

$$z_o = W_o \cdot a_h + b_o \tag{7}$$

$$a_o = \sigma(z_o) \tag{8}$$

where, z_h is the weighted input for the hidden layer; W_h is the weight matrix from the input layer to the hidden layer; x is the input vector; b_h is the bias vector for the hidden layer; a_h is the activation output of the hidden layer, and σ is the activation function; z_o is the weighted input for the output layer; W_o is the weight matrix from the hidden layer to the output layer; b_o is the bias vector for the output layer, and a_o is the final output of the network.

During backward propagation, the error between the predicted values for sample x and the actual labels is calculated based on the current network weights (Equations 9 and 10). The weights and biases of each layer are then updated in reverse to adapt to changes in the external environment (Equations 11 and 12). Training is considered complete after multiple cycles, ensuring that the final output closely matches the target value.

$$\delta_o = (a_o - y) \times \sigma'(z_o) \tag{9}$$

$$\delta_h = (W_o^T \cdot \delta_o) \times \sigma'(z_h) \tag{10}$$

$$W_o = W_o - \eta \cdot \delta_o \cdot a_h^T \tag{11}$$

$$W_h = W_h - \eta \cdot \delta_h \cdot x^T \tag{12}$$

where, δ_o is the error of the output layer; y is the actual label; σ' is the derivative of the activation function of the output layer; δ_h is the error of the hidden layer; W_o^T is the transpose of the weights from the output layer to the hidden layer; η is the learning rate.

The neural network models presented in this study were developed and tested using the MATLAB 2022a software (MathWorks, Natick, MA, USA) environment.[27]

4.2. BP neural network structure selection

Hecht-Nielsen laid a robust theoretical foundation for single-hidden-layer feedforward neural networks. He posits that such networks can approximate any continuous function on a finite closed set with arbitrary accuracy, given a sufficient number of hidden layer neurons and an appropriate activation function. To mitigate model complexity and prevent overfitting, this study employs a single hidden layer. Insufficient neurons in the hidden layer can cause underfitting, whereas an excessive number may lead to overfitting. The hidden layer neuron count was determined using the empirical formula (13) [28].

$$n_l = \sqrt{m+n} + a \tag{13}$$

where, n_l is the number of neurons in the hidden layer; m is the number of neurons in the input layer of the network; n is the number of neurons in the output layer of the network; a is an integer between [1-10].

To improve the network's capability in managing nonlinear expressions and to enhance its generalization, this study employs the tansig function as the activation function for the hidden layer and the pureline function for the output layer[29,30].

$$\text{tansig}(x) = \frac{2}{1+e^{-2x}} - 1 \tag{14}$$

$$\text{purelin}(x) = x \tag{15}$$

The BP neural network prediction model presented in this paper takes four structural dimension parameters that influence the mechanical performance of the brake ring as input values: ring diameter D, tube diameter d, tube wall thickness T, and aluminum sleeve length L. The model outputs three mechanical performance indicators derived from the trilinear load-displacement curve within the effective displacement range of the brake ring: starting load F_1, maximum load F_3, and energy dissipation E.

Given the simple data structure in this project, the dataset is divided into 85% for training and 15% for testing, based on random selection. The training set includes the training sample set X1 and the training label set Y1. The test set comprises the test sample set X2 and test label set Y2. X1 and Y1 contain 489 pairs of samples and labels, while X2 and Y2 contain 87 pairs of samples and labels. The number of training iterations is set to 1000, and the learning rate is set to 0.01.

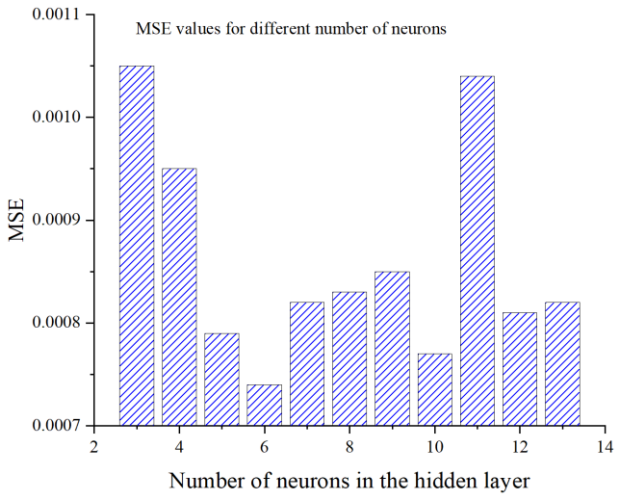

Fig. 14 MSE under different number of hidden layer neurons

To determine the optimal number of neurons within the range determined by empirical formulas, the Mean Squared Error (MSE) values (Formula 16) for multi-output with different neuron counts, ranging from 3 to 15, were plotted in Fig. 14. Based on the experimental data, the minimum multi-output Mean Squared Error occurs when the hidden layer contains six neurons. Therefore, the optimal number of neurons for the hidden layer is determined to be $n_l = 6$, at which the MSE is minimized. The BP neural network model structure in this paper is 4-6-3.

$$MSE = \frac{1}{S}\sum_{k=1}^{S}\left(\frac{1}{N}\sum_{i=1}^{N}\left(y_{ki} - y_{ki}^{'}\right)^2\right) \tag{16}$$

where, N is the number of samples; y_{ki} is the kth predicted output parameter in the ith sample; $y_{ki}^{'}$ is the kth actual output parameter in the ith sample; S is the number of neurons in the output layer, and S is 3 in this paper.

5. Validation of the model for predicting mechanical properties of the brake ring

5.1. Indicators for the assessment of the model

The evaluation metrics for the BP neural network model primarily involve the measurement of prediction accuracy and the model's generalization ability. This paper uses the Root Mean Square Error (RMSE) and the Coefficient of Determination (R^2) as the performance evaluation indicators for the BP neural

network model. The calculation formulas for RMSE and R^2 are:

$$RMSE = \sqrt{\frac{1}{N}\sum_{i=1}^{N}\left(y_i - y_i^{'}\right)^2} \tag{17}$$

$$R^2 = 1 - \frac{\sum_{i=1}^{N}\left(y_i - y_i^{'}\right)^2}{\sum_{i=1}^{N}\left(y_i - \bar{y}\right)^2} \tag{18}$$

where, N is the number of samples; y_i is the predicted value by the model; $y_i^{'}$ is the actual target value of the sample; $\bar{y}$ is the average actual target value of the samples.

5.2. Validation of the model

The accuracy of the BP neural network prediction model is crucial for subsequent reverse structural dimension design based on target mechanical performance. To precisely design brake ring dimensions, it is necessary to adjust neural network parameters multiple times and select the prediction model with the highest accuracy. The training results shown in Fig. 15 indicate that the coefficient of determination (R^2) for all samples reached 0.991, demonstrating high model fidelity. The predicted output values can be approximately considered as the actual outputs of a nonlinear function, meeting the accuracy requirements of the training.

Fig. 16 shows the test set prediction results for various mechanical performance parameters. In the test set, the Root Mean Square Errors (RMSE) for the starting load F_1, maximum load F_3, and energy dissipation E were 1.76 kN, 3.23 kN, and 1.57 kJ, respectively, with prediction accuracies of 97.6%, 96.5%, and 98.8%.

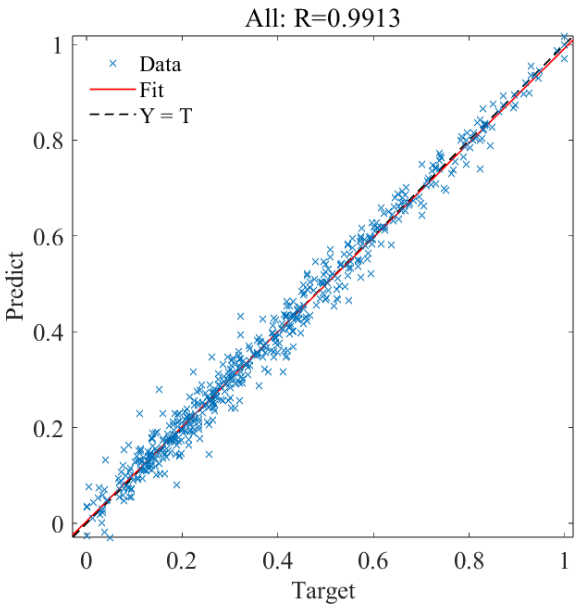

Fig. 15 BP neural network all sample regression results

In the final stages of stretching, the brake ring undergoes significant deformation, with most materials entering the plastic phase. Once the steel tube's diameter reduces to a certain extent, torsional deformation increases component stiffness, significantly increasing the maximum load. Significant deformation in the final calculation stages leads to instability issues, causing variability in the maximum load and greater errors compared to the starting load. However, the energy dissipation of the brake ring is mainly due to the sliding deformation before the load reaches F_2. Therefore, the error from the abrupt change in maximum load has little impact on energy dissipation.

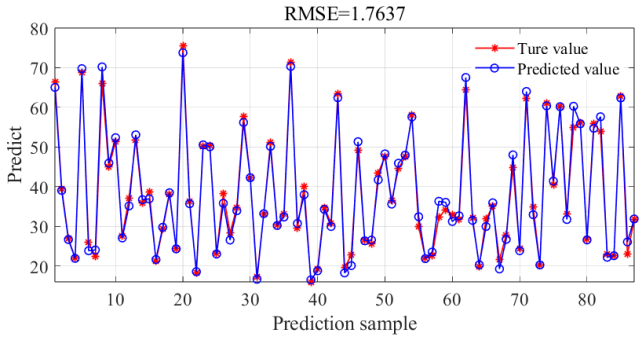

(a) Starting load F_1

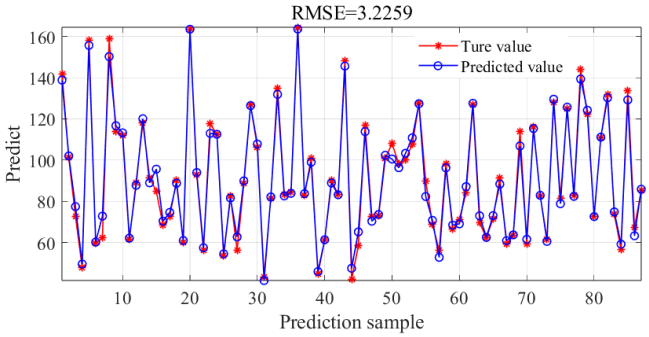

(b) Maximum load F_3

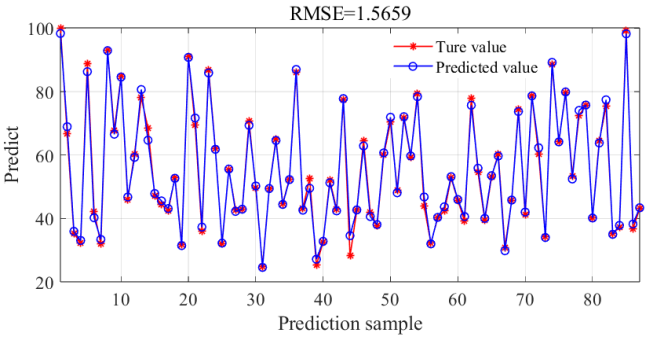

(c) Energy dissipation E

Fig. 16 BP neural network prediction and label comparison

6. Reverse design of brake ring based on PSO algorithm

6.1. Particle Swarm Algorithm

Particle Swarm Optimization (PSO) is a heuristic global optimization technique inspired by the foraging behavior of bird flocks[31,32]. In the PSO algorithm, each "bird" is termed a "particle," and a certain number of particles are randomly generated initially to form a population. Each particle in the population is a vector with multiple spatial dimensions, each having a position and velocity within the search space. Each particle in the population is a vector with multiple spatial dimensions, each having a position and velocity within the search space. The detailed process is illustrated in Fig. 17.

$$\begin{aligned} v_i(t+1) = {} & w \times v_i(t) + c_1 \times rand_1 \times (pbest_i - x_i(t)) + \\ & c_2 \times rand_2 \times (gbest - x_i(t)) \end{aligned} \tag{19}$$

$$x_i(t+1) = x_i(t) + v_i(t+1) \tag{20}$$

where, $v_i(t)$ represents the velocity of particle x_i at time t; $x_i(t)$ represents the position of particle i at time t; ω is the inertia weight; c_1 and c_2 are learning factors; $rand$ is a random number within the interval [0,1]; $pbest_i$ and $gbest$ respectively represent the best position encountered so far by particle i and the best position encountered by all particles to date.

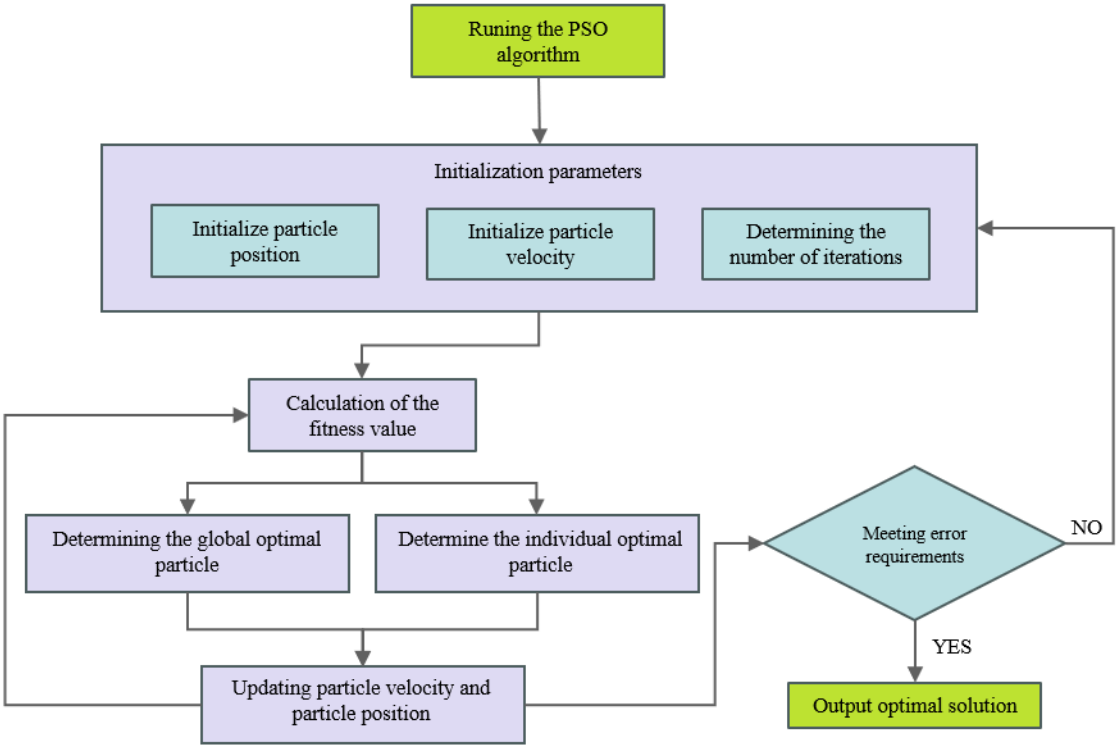

Fig. 17 Flowchart of PSO algorithm

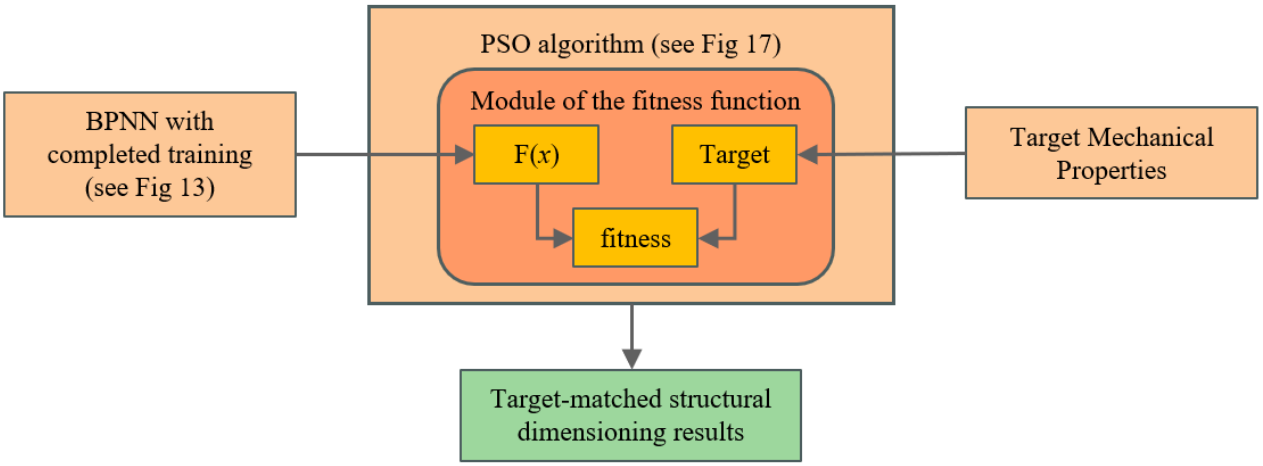

Fig. 18 Flowchart of BPNN-PSO Reverse Design

The fitness value represents the quality of each particle as the best structural dimension design result that matches the target mechanical performance. This paper employs Eq. (21) as the fitness function. A lower fitness value indicates that the particle is closer to the optimal solution. Through multiple iterations of updates, the particle closest to the target is identified.

$$fit(x) = \frac{1}{S}\sum_{k=1}^{S}(y(x)_k - y_k^{'})^2 \tag{21}$$

where, x is the input parameter vector; S represents the number of neurons in the output layer, which in this paper is set to 3; $y(x)_k$ is the *kth* predicted output value for the input parameter x ; $y_k^{'}$ is the *kth* value of the target mechanical performance parameters.

6.2. PSO parameters selection

In the forward prediction model, inputting four structural dimension features allows the prediction of three mechanical performance indicators of the brake ring. In the reverse design problem, which targets optimal structural dimensions based on desired mechanical performance, a population of structural dimension parameters is randomly generated using the forward prediction model. The individual and global optimal particles are determined based on each particle's fitness value within the population. Finally, through continuous iterations and optimization, the structural dimension parameters that best match the target mechanical performance are obtained.

From the input parameters of the BP neural network prediction model, the spatial dimension number M for the PSO algorithm's particle swarm is determined to be four dimensions. This means the position vector of particle individuals can be represented as $x_i = (x_1, x_2, x_3, x_4)_i$, and the velocity vector as $v_i = (v_1, v_2, v_3, v_4)_i$. Both the individual learning factor and the social learning factor are set to 2. The inertia weight is set to a constant value of 1. The particle swarm size is set to 5, and the number of iterations to 100[33].

6.3. Structural dimension design of brake ring based on target mechanical performance

The ring diameter of the brake ring determines its effective sliding distance during stretching process. To systematically categorize brake rings with different effective sliding distances, the reverse design model discretizes the

ring diameter, fixing the values at 400mm, 450mm, 500mm, and 550mm, corresponding to effective sliding distances of 900mm, 1000mm, 1100mm, and 1200mm, respectively. Typically, brake rings with different structural size combinations can have similar mechanical properties. This means that for specific mechanical performance, there is no unique optimal solution for the brake ring; multiple local optima can exist.

In the reverse design model, the basic process is: ① Specify the mechanical performance indicators of the brake ring, including the required starting load, maximum load, and energy dissipation; ② Import the forward mechanical performance prediction model of the brake ring, randomly generating a population of potential optimal structural dimensions; ③ Set up a fitness function, calculate the fitness value of each particle, and use the Particle Swarm Optimization algorithm to iteratively update to the optimal solution; ④ Repeat the above process to output multiple design dimensions. The key step in this process is introducing the trained neural network as the fitness calculation function in the PSO optimization algorithm, as shown in Fig. 18.

For a specific target mechanical performance, such as a starting load of 40kN, a maximum load of 85kN, and energy dissipation of 54kJ, the reverse design model outputs four different structural dimension combinations, as shown in Table 5. The fitness iteration curve of the design process is shown in Fig. 19.

Table 5
Design of brake ring structure size

Number	*D*/mm	*d*/mm	*T*/mm	*l*/mm
1	450	41.96	3.49	80.25
2	450	41.73	4.40	66.67
3	500	36.23	2.58	120.00
4	550	30.00	4.07	120.00

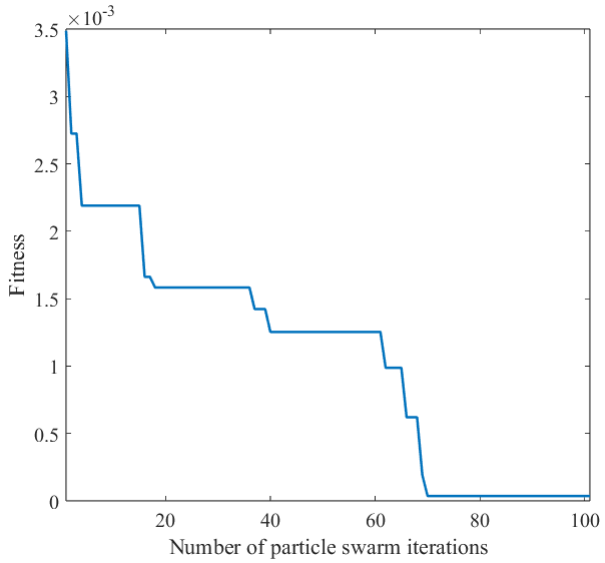

Fig. 19 Fitness value iteration curve

6.4. Mechanical Testing and Numerical Simulation Validation of the Brake Ring Design Model

To verify the effectiveness of the reverse design model, two sets of mechanical tests and numerical simulations were conducted using the structural dimension combination with serial number 1 as an example. The designs of the remaining serial numbers were verified for validity using numerical simulations.

During the mechanical testing process, the actual structural dimensions of the brake ring were: ring diameter of 450 mm, tube diameter of 42 mm, tube wall thickness of 3.5 mm, and aluminum sleeve length of 80 mm. The testing equipment utilized a vertical tensile testing machine with a capacity of 150 tons and a hydraulic cylinder travel of 2500 mm. It was equipped with force and displacement sensors, as shown in Fig. 20. The lower end of the brake ring's wire rope was attached to a shackle fixed to a steel beam anchored to the ground, while the upper end was connected to a shackle fixed to the tensile arm of the testing machine. During the stretching process, force and displacement data were recorded every 0.2 seconds, resulting in the force-displacement curve shown in Fig. 21. Concurrently, a numerical model was established using the designed structural dimensions to perform a numerical simulation analysis of the brake ring, comparing and verifying the reliability of the reverse design model.

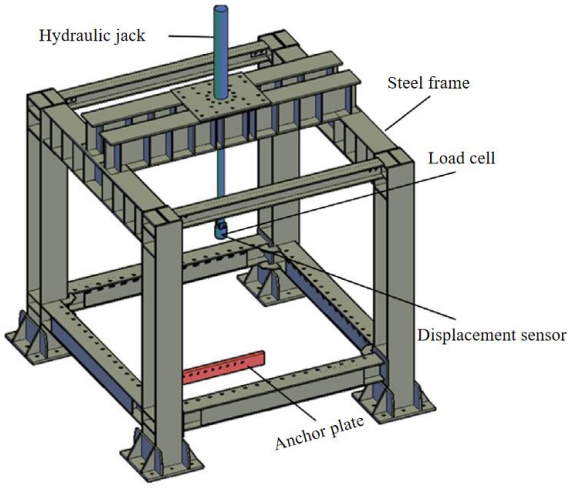

Fig. 20 Quasi-static tensile testing machine

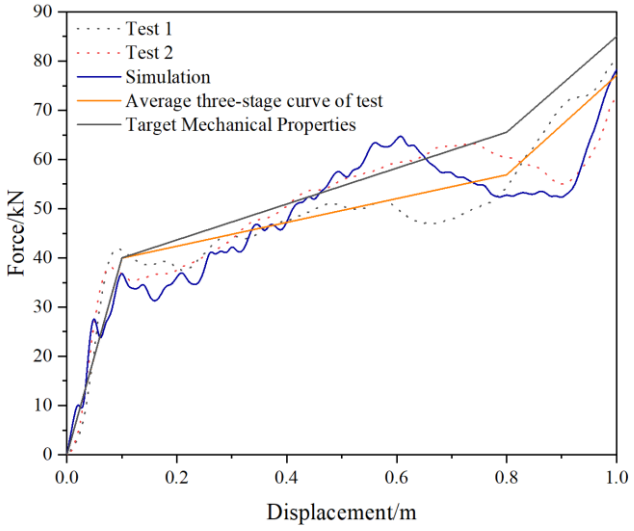

Fig. 21 Comparison of the target, mechanical tests, and simulation results of brake ring

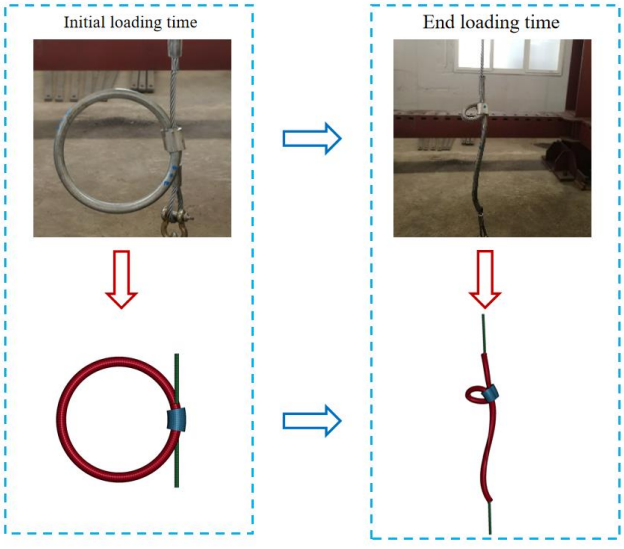

Fig. 22 Comparison of test and simulation deformation for brake ring No. 1

As shown in Table 6, the errors between the experimental results and the target performance for the three mechanical indicators in Design 1 are -0.25%, -9.29%, and -8.89%, respectively, based on both experimental and numerical simulation analysis. Additionally, the numerical simulation aligns with the experimental results, further validating the effectiveness of the design method. For Designs 2, 3, and 4, only numerical simulation validation was conducted. The comparisons of their load-displacement curves with the target performance are shown in Fig. 23, and the result analysis is provided in Table 7.

In summary, the structural dimensions of the brake ring designed according to specific mechanical performance criteria result in actual products whose mechanical performance indicators and numerical simulation results have errors within 10% of the required targets, all within an acceptable engineering range. This achieves a high-precision design, ensuring that the actual structural dimensions of the brake ring meet the required mechanical performance targets.

Table 6
Mechanical test, numerical simulation and target performance analysis of the designed brake ring

Case	F_1(Kn)	F_3(kN)	E(kJ)
Test 1	41.8	80.8	50.2
Test 2	38.1	73.4	48.3
Test Average	39.9	77.1	49.2
Simulation	38.0	78.3	49.2
Target	40.0	85.0	54.0
Test results and target error	-0.25%	-9.29%	-8.89%

Table 7
The numerical simulation results analysis of other designs

Case	F_1(mm)	F_3(mm)	E(mm)	Error F_1	Error F_3	Error E
Design 2	39.0	87.1	55.5	-2.50%	2.47%	2.78%
Design 3	37.3	88.6	58.2	-6.75%	4.23%	7.78%
Design 4	37.7	87.8	58.0	-5.75%	3.29%	7.41%
Target	40.0	85.0	54.0	--	--	--

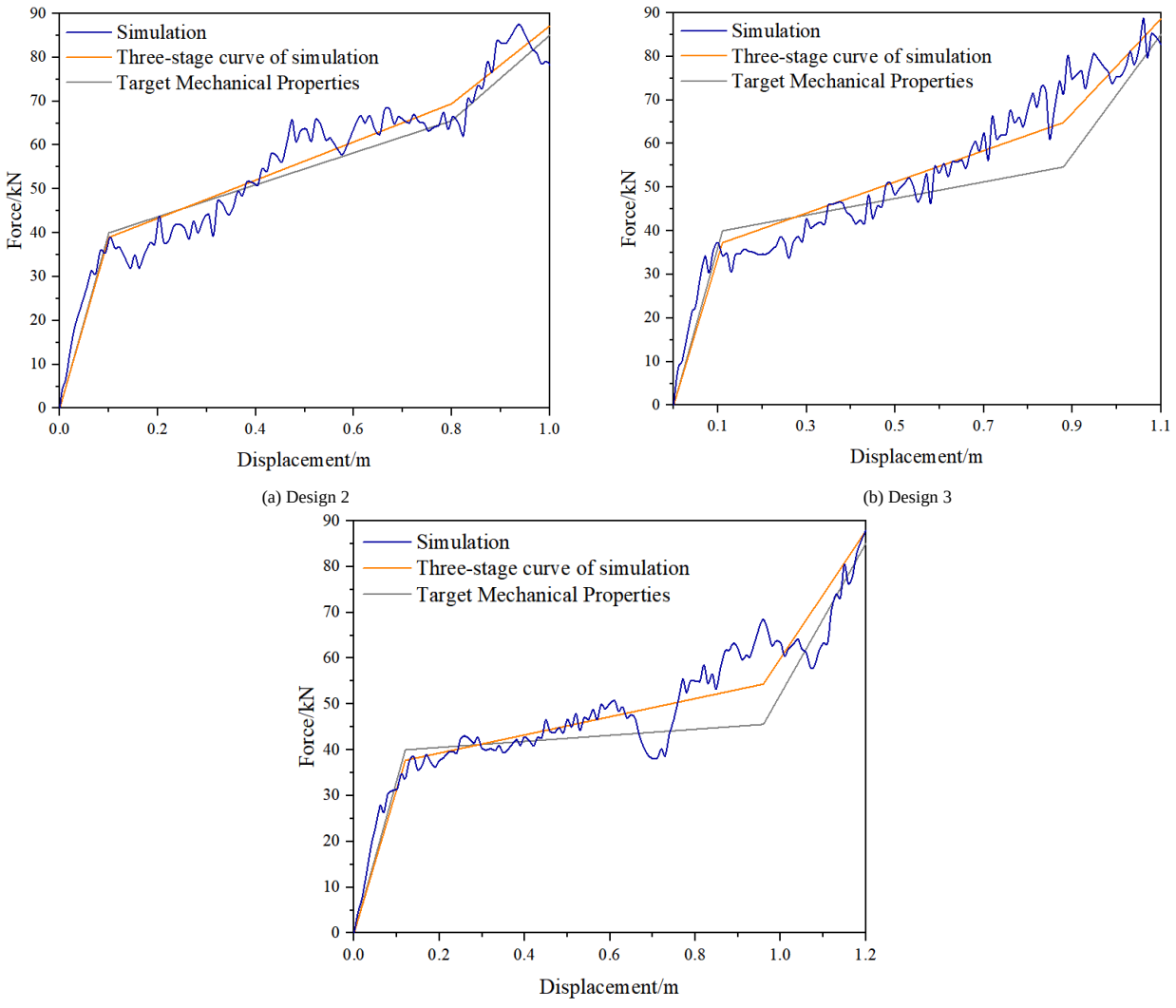

(a) Design 2

(b) Design 3

(c) Design 4

Fig. 23 Numerical simulation results of remaining designs compared to target performance.

7. Conclusions

This paper establishes a brake ring mechanical performance prediction model and a reverse design model based on target mechanical performance using the BP neural network and PSO optimization algorithm, leading to the following important conclusions:

(1) The mechanical performance of the brake ring is mainly influenced by its structural dimensions, including ring diameter, tube diameter, tube wall thickness, and aluminum sleeve length. The BP neural network designed in this study, with an input layer of 4 nodes, a hidden layer of 6 nodes, and an output

layer of 3 nodes, effectively reflects the nonlinear mapping relationship between the brake ring's structural dimensions and mechanical performance.

(2) Through comparison and verification between actual product tests and numerical simulation results of the brake ring, the BP neural network-based prediction model and the PSO algorithm-based reverse design model proposed in this paper can design brake rings that meet specific mechanical performance requirements for engineering projects, offering a practical method for selecting energy dissipators in flexible protection systems.

(3) The successful application of the automated design method for energy dissipators in flexible protection systems proposed in this paper can be extended to other components. Future research will focus on the automated design of both individual components and the overall structure of flexible protection systems.

Acknowledgements

This study is supported by the Sichuan Science and Technology Program (Grant No. MZGC20240052).

References

[1] Yang J, Duan S, Li Q, et al. A review of flexible protection in rockfall protection. Natural Hazards, 2019, 99: 71-89.
[2] JIN Yuntao, YU Zhixiang, LUO Liru, et al. A study on energy dissipation mechanism of a guided flexible protection system under rockfall impact. Journal of Vibration and Shock, 2021, 40 (20): 177-185+192.(in Chinese)
[3] LIU Zhanhui, LU Zhimou, LI Yongle, et al. Study on Impact Resistance of Flexible Shed Tunnel for Bridges in Mountainous Areas. Journal of The China Railway Society,2023,45(03):129-136. (in Chinese)
[4] Muraishi H, Samizo M, Sugiyama T. Development of a flexible low-energy rockfall protection fence. Quarterly Report of RTRI, 2005, 46(3): 161-166.
[5] Castro-Fresno D, Del Coz Díaz J J, Nieto P J G, et al. Comparative analysis of mechanical tensile tests and the explicit simulation of a brake energy dissipater by FEM. International Journal of Nonlinear Sciences and Numerical Simulation, 2009, 10(8): 1059-1085.
[6] Lambert S, Nicot F. Multi-scale analysis of an innovative flexible rockfall barrier. 2013.
[7] del Coz Díaz J J, Nieto P J G, Castro-Fresno D, et al. Nonlinear explicit analysis and study of the behaviour of a new ring-type brake energy dissipator by FEM and experimental comparison. Applied Mathematics and Computation, 2010, 216(5): 1571-1582.
[8] Castanon-Jano L, Blanco-Fernandez E, Castro-Fresno D, et al. Energy dissipating devices in falling rock protection barriers. Rock Mechanics and Rock Engineering, 2017, 50: 603-619.
[9] QI Xin, XU Hu, YU Zhixiang, et al. Dynamic mechanical property study of break rings in Flexible Protective System. Engineering Mechanics, 2018, 35(9):9. (in Chinese)
[10] Lu XZ, Liao WJ, Zhang Y, Huang YL, Intelligent structural design of shear wall residence using physics-enhanced generative adversarial networks, Earthquake Engineering & Structural Dynamics, 2022, 51(7): 1657-1676.
[11] Zhao PJ, Liao WJ, Huang YL, Lu XZ, Intelligent beam layout design for frame structure based on graph neural networks, Journal of Building Engineering, 2023, 63, Part A: 105499.
[12] Bao Yuequan, Li Hui. Artificial Intelligence for Civil Engineering. China Civil Engineering Journal, 2019, 52(5): 1-11. (in Chinese)
[13] Joshi D A, Menon R, Jain R K, et al. Deep learning-based concrete compressive strength prediction model with hybrid meta-heuristic approach. Expert Systems with Applications, 2023, 233: 120925.
[14] Yi Peng, Xinyi Yu, Yixin Huang, et al. Asphalt pavement raveling recognition based on deep learning algorithms, Intelligent Transportation Infrastructure, 2024.
[15] Yongding Tian, Junhao Zhang, et al. Comprehensive review of noncontact sensing Technologies for Bridge Condition Monitoring and Assessment, Intelligent Transportation Infrastructure, 2024.
[16] Chen W, Xu J, Dong M, et al. Data-driven analysis on ultimate axial strain of FRP-confined concrete cylinders based on explicit and implicit algorithms. Composite Structures, 2021, 268: 113904.
[17] Xu J, Chen Y, Xie T, et al. Prediction of triaxial behavior of recycled aggregate concrete using multivariable regression and artificial neural network techniques. Construction and Building Materials, 2019, 226: 534-554.
[18] Pham T M, Hadi M N S. Predicting stress and strain of FRP-confined square/rectangular columns using artificial neural networks[J]. Journal of Composites for Construction, 2014, 18(6): 04014019.
[19] MA Gao, LIU Kang. Prediction of Compressive Strength of CFRP-confined Concrete Columns Based on BP Neural Network. Journal of Hunan University(Natural Sciences) ,2021,48(09):88-97.
[20] ZHOU Zhong, ZHANG Junjie, et al. Prediction model of sewage treatment in tunnel green construction based on PSO-BP neural network. Journal of Railway Science and Engineering, 2022, 19(5): 1450-1458. (in Chinese)
[21] Liao L, Yu Z, Yang X, et al. An automated computation method for flexible protection systems based on neural networks. Computers and Geotechnics, 2024, 165: 105932.
[22] Cascardi A, Micelli F, Aiello MA. An Artificial Neural Networks model for the prediction of the compressive strength of FRP-confined concrete circular columns. Eng Struct 2017;140:199–208.
[23] Jiang K, Han Q, Bai Y, Du X. Data-driven ultimate conditions prediction and stress-strain model for FRP-confined concrete. Compos Struct 2020;112094.
[24] WANG Min, SHI Saoqing, YANG Youkiu. Static tensile test and FEM dynamic simulation for a ring-brake energy dissipater. Journal of Vibration and Shock,2011,30(04):188-193. (in Chinese)
[25] TIAN Zhenhua, SHI Shaoqing, et al. Mechanical Testing on the Ring-brake Energy Dissipater and Influence of Thickness on Its Energy Dissipation Performance. Journal of Logistical Engineering University, 2014, 30(3): 8-12. (in Chinese)
[26] LIU Chengqing, CHEN Linya, CHENG Chi, et al. Full scale test and FEM simulation to ring-type brake energy dissipater in falling rock protection. Chinese Journal of Rock Mechanics and Engineering, 2016, 35(6): 1245-1254. (in Chinese)
[27] The MathWorks. <http://www.mathworks.com/products/matlab/>; 2007.
[28] DAI Yimin, LI Yixin, XU Ying, et al. Prediction of hail impact force induced by Wind-Hail coupling based on GA-BP Neural Network. Engineering Mechanics, 2024. 1-10. (in Chinese)
[29] CHENG Qing, MA Rui, JIANG Zhengwu, et al. Compressive Strength Prediction and Mix Proportion Design of UHPC Based on GA-BP Neural Network. Journal of Building Materials, 2020, 23(1): 176-183+191.(in Chinese)
[30] CHEN W, XU J, DONG M, et al. Data-driven analysis on ultimate axial strain of FRP-confined concrete cylinders based on explicit and implicit algorithms. Composite Structures, 2021, 268: 113904.
[31] POLI R, KENNEDY J, BLACKWELL T. Particle swarm optimization: An overview. Swarm Intelligence, 2007, 1(1): 33-57.
[32] LI Guangbao, GAO Dong, LU Yong, et al. Internal surface treatment of gas-liquid-solid technology based on PSO-BP algorithm and FLUENT. Journal of Jilin University (Engineering and Technology Edition), 2024, 1-12. (in Chinese)
[33] YANG Junqi, FAN Xiaojun, ZHAO Yuehua, et al. Prediction of carbon emissions in Shanxi Province based on PSO-BP neural network. Journal of Environmental Engineering Technology: 1-15. (in Chinese)